MIMO Radar Calibration and Imagery for Near-Field Scattering Diagnosis

YONGZE LIU
XIAOJIAN XU
GUANGYAO XU
School of Electronics and Information Engineering, Beihang University, Beijing 100191, China

Multiple-input multiple-output (MIMO) radar is an enabling technique for high-resolution imaging, which is especially useful for near-field electromagnetic scattering diagnosis of complex targets. Among others, high sidelobes and radar cross section (RCS) calibration uncertainty are the major challenges for such applications, due to array nonuniformity, imperfect channels, and antenna pattern tapering. These shortcomings prevent a MIMO radar from obtaining high-quality images with enough dynamic range and RCS accuracy. In this paper, we develop a complete solution for these problems. A novel adaptive weighting technique is proposed, where the complex weights are optimized for exact amplitude and phase error calibration of a MIMO array and for azimuth sidelobe reduction. A MIMO filtered backprojection algorithm is developed for image formation with improved RCS calibration accuracy, where propagation path-loss, antenna pattern tapering, and phase distortion due to the near-field spherical wave front are compensated. Both indoor and outdoor field test results are presented to show the high-quality images obtained using the proposed techniques, demonstrating the applicability of a MIMO radar for diagnostic RCS imaging of complex targets.

Manuscript received December 18, 2016; revised May 15, 2017 and September 11, 2017; released for publication September 12, 2017. Date of publication October 9, 2017; date of current version February 7, 2018.

DOI. No. 10.1109/TAES.2017.2760758

Refereeing of this contribution was handled by S. Watts.

This work was supported in part by the National Natural Science Foundation of China under Grant 61371005.

Authors' addresses: Y. Liu, X. Xu, and G. Xu are with the School of Electronics and Information Engineering, Beihang University, Beijing 100191, China, E-mail: (liuyongze68@eyou.com; xiaojianxu@buaa.edu.cn; guxingleiyy@126.com). *(Corresponding author: Xiaojian Xu.)*

I. INTRODUCTION

Rail synthetic aperture radar (SAR) [1], [2] and turntable inverse SAR (ISAR) [3], [4] are commonly used for high-resolution diagnostic imaging of complex targets and radar cross section (RCS) measurement. Both techniques require long data acquisition time, due to the fact that either mechanical scanning or turntable rotation is required.

Multiple-input multiple-output (MIMO) radar [5]–[13] is an enabling technique capable of imaging a target using only one snapshot. A MIMO radar makes use of a small number of antennas to configure a sparse array, which solves the problem of grating lobes despite the large element spacing. Furthermore, the complexity of the system can be reduced to an achievable level. In combination with wideband signals, high resolutions in both down-range and cross-range dimensions are obtained. The main feature of MIMO radar is that the transmitted signals from all transmitters can be completely separated at each receiver. Three schemes [14]–[25] can be implemented for this. The first is the waveform diversity (WD) technique [14]–[23], which has received more attention for target detection applications, where orthogonal waveforms are radiated from transmitters and recovered at receivers through a bank of matched filters. Meanwhile, nonorthogonal waves, as illustrated in [16]–[18], can also be employed for WD and to enhance detection probability or parameter estimation accuracy [19]. In addition, for colocated MIMO configurations, it is possible to suitably shape the beampattern [20]–[22]. However, in a practical radar system, it is difficult to define perfectly orthogonal wideband waveforms and to mitigate the effects of cross correlation between received signals. As a consequence, WD is not currently suitable for diagnostic imaging, where a large dynamic range is a must. The second is based on frequency diversity, meaning that signals in different frequency bands or subbands do not overlap with each other. Therefore, these signals can be transmitted simultaneously using different transmit elements, as discussed in [23]. The third is time-division multiplexing (TDM) across transmit and receive elements through switch matrices [24], [25], otherwise known as time diversity. This outperforms the WD mode in terms of signal separation, but does increase the data acquisition time to some extent. However, for the measurement of stationary targets, this increase in time is insignificant.

The vast majority of MIMO radar imaging systems for various applications operates in TDM mode. Examples include the SIRE forward-looking radar [26], [27], the UWB switched-antenna-array imaging system [25], [28], the ARTINO three-dimensional (3-D) imaging radar [29], [30], and the MELISSA system [31]. MIMO radar imaging has also attracted the attention of researchers engaged in RCS measurement. Massaloux and Bérisset [32] were the first to present the MIMO radar image of a metallic cylinder, where experimental data were acquired from a MIMO array consisting of 14 transmitting and receiving antennas. It was shown that the resulting image has good similarity with its turntable ISAR counterpart. Stewart *et al.* [33] carried out a series of MIMO radar imaging experiments using waveform-diverse and time-diverse modes, where the coded pseudonoise (PN), the combination of PN and FD, and the linear frequency-modulated waveforms were used as transmitted signals. The resulting images of a metallic sphere for all waveforms in [33] show good agreement between WD and TDM. However, the authors also pointed out that the measurement results for two trihedral reflectors show higher average noise level than the result of the sphere in WD mode.

Image dynamic range is of special importance for high-resolution scattering diagnosis of complex targets. From the literature [25]–[28], [31], [33]–[35], the dynamics of the MIMO images from measured data are about 30 dB, which limits the applications for target scattering diagnosis. Generally, sidelobes in down-range dimension can be successfully reduced by applying a conventional amplitude weighting function to the frequency domain data. However, amplitude weighting is not effective for azimuth sidelobe reduction. This is due to the fact that the amplitude and phase of the return data have been destroyed due to the system hardware imperfection. As a consequence, high sidelobes are one of the major challenges. In addition, unlike real-beam radars where array pattern synthesis [20]–[22] is used for one-way suppression of sidelobes, a wide field of view is required for MIMO radar near-field imaging and the responses of the MIMO array to all returns from different directions must have lower sidelobes. RCS calibration uncertainty is another challenge for near-field target measurements due to antenna pattern tapering of transmit and receive elements.

This paper focuses on producing high-resolution MIMO radar images of diagnostic quality by developing a complete signal processing solution. To this end, an adaptive weighting technique is proposed for amplitude and phase error calibration of a MIMO array and for azimuth sidelobe reduction. Then, a MIMO filtered back-projection (MIMO-FBP) algorithm is refined for precision image formation with improved RCS calibration accuracy, where propagation path-loss, antenna pattern tapering, and phase distortion due to the near-field spherical wave front are compensated. An experimental MIMO radar system is developed and used for both indoor and outdoor field tests. Images with high dynamics are obtained, demonstrating the applicability of a MIMO radar for diagnostic RCS imaging of complex targets.

The remainder of this paper is organized as follows. The configuration of the MIMO array and the signal model are discussed in Section II. Section III focuses on the amplitude and phase error calibration of a MIMO array with azimuth sidelobe reduction. Section IV pays more attention to develop a near-field MIMO imaging algorithm for precision RCS imaging. In Section V, an experimental MIMO radar is developed. Indoor and outdoor field test results are presented together with detailed analyses. We conclude this paper in Section VI.

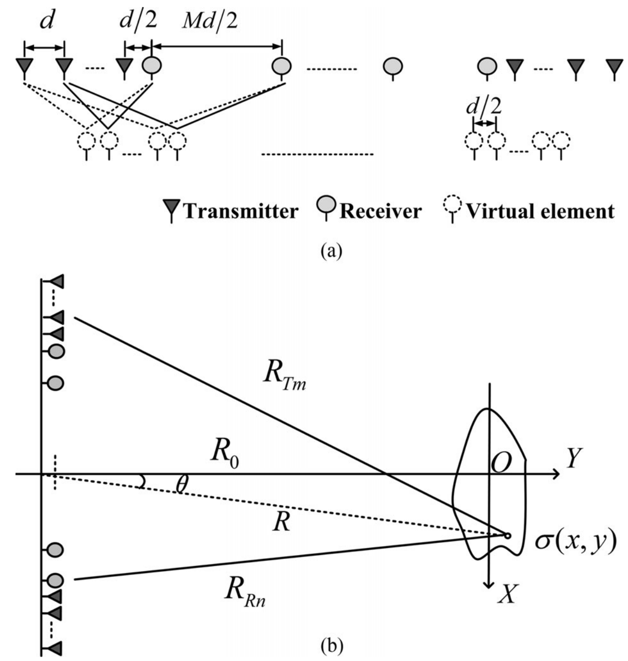

Fig. 1. Configuration of MIMO array and near-field imaging geometry. (a) MIMO array. (b) Imaging geometry.

II. SYSTEM CONFIGURATION AND SIGNAL MODEL

MIMO radar has the capability of snapshot data acquisition. For near-field imaging applications, it makes use of closely spaced transmit and receive antennas to configure a MIMO array [36], [37] so that a large virtual aperture may be synthesized. In combination with wideband signals, high resolutions in both down-range and cross-range dimensions can be obtained.

A. System Configuration

Details of the MIMO array configuration used here are shown in Fig. 1(a), where the transmit elements are divided into two groups placed at the two ends of the array, while the receive elements are uniformly located in the middle of the array. Suppose that the MIMO array consists of M transmit elements and N receive elements, such that $M \times N$ virtual elements are synthesized. The interspacing of the transmit and the receive elements are set to be d and $Md/2$, respectively. The spacing between the transmit and the receive array is $d/2$. For far-field measurement, the virtual array synthesized by such a configuration is equivalent to a linear equispaced array, and the aperture utilization ratio is higher compared to most other configurations. However, for near-field imaging applications, the virtual array cannot be considered to be perfectly linearly equispaced [25].

The down-range resolution is determined by the frequency bandwidth of the transmitted waveform and is expressed as

$$\rho_r = \frac{c}{2B} \tag{1}$$

where c is the speed of propagation, and B denotes the frequency bandwidth.

The cross-range resolution can be estimated as [38], [39]

$$\rho_c \approx \frac{\lambda R}{2L_{\mathrm{vir}}} \tag{2}$$

where λ is the wavelength, R is the distance from the scatterer to the center of MIMO array, and L_{vir} is the length of virtual aperture, which is proportional to the length of the physical MIMO array.

For a linear equispaced array, element spacing is generally required to be less than half a wavelength. However, for many specific applications, such criteria cannot be satisfied, resulting in grating lobes due to under sampling across the aperture dimension. The grating lobes of the MIMO array are determined by the virtual element spacing as [40]

$$\theta_{\mathrm{gl}} \approx \arcsin\left(\frac{\lambda}{2d_{\mathrm{vir}}}\right) \tag{3}$$

where θ_{gl} is the position of the grating lobe relative to the mainlobe, and d_{vir} is the spacing between the virtual elements.

Near-field imaging geometry is shown in Fig. 1(b), where the MIMO array is parallel to the $X-$axis. R_0 is the reference distance from the center of the MIMO array to the origin in the target coordinate system; R_{Tm} is the path from the mth transmit element to the scatterer σ, and R_{Rn} is the path from σ to the nth receive element. Scatterer position is represented by (x, y) in a target coordinate system OXY or by (R, θ) in a radar polar coordinate system, where $R = \sqrt{x^2 + (y + R_0)^2}$ and $\theta = tg^{-1}(x/(R_0 + y))$.

B. Signal Model

Suppose that each transmit element radiates a stepped-frequency pulse-train signal [41], i.e.,

$$s_m(t) = \sum_{k=1}^{K} u(t - kT_r)e^{j2\pi f_k t} \tag{4}$$

where s_m denotes the signal transmitted by the mth element, K is the number of pulses, f_k is the carrier frequency of the kth pulse, T_r is the pulse repetition interval, and $u(t)$ is a rectangular pulse.

The propagation delay from the mth transmitter to the scatterer σ and then back to the nth receiver can be expressed as

$$\tau = \frac{R_{Tm} + R_{Rn}}{c} \tag{5}$$

where $R_{Tm} = \sqrt{(x - x_{Tm})^2 + (y + R_0)^2}$, $R_{Rn} = \sqrt{(x - x_{Rn})^2 + (y + R_0)^2}$, x_{Tm}, and x_{Rn} are the positions of the mth transmit and the nth receive elements, respectively, on the X–axis.

To simplify the expression, the propagation path-loss and element pattern are neglected in the following equations. The return of the kth pulse received by the nth receive element can then be represented as

$$s_{mn}(t) = s_m(t - \tau) = \sigma(x, y)u(t - kT_r - \tau)e^{j2\pi f_k(t-\tau)} \tag{6}$$

where $\sigma(x, y)$ is the target scattering function, which is assumed to be independent of the frequency and aspect direction of the incident field. The RCS of the scatterer at (x, y) is the square of the scattering function $\sigma(x, y)$.

The reference signal at the radar receiver is the delayed signal of the kth pulse, namely, $s_m(t - \tau_0) = u(t - kT_r - \tau_0)e^{j2\pi f_k(t-\tau_0)}$, where $\tau_0 = 2R_0/c$. Therefore, the output of the receiver is the cross-correlation function of the reference signal relative to the received return signal, i.e.,

$$\begin{aligned} s_{mn}(f_k) &= s_{mn}(t)s_m^*(t - \tau_0) \\ &= \sigma(x, y)e^{-j\frac{4\pi f_k}{c}\left(\frac{R_{Tm}+R_{Rn}}{2} - R_0\right)} \end{aligned} \tag{7}$$

where * denotes complex conjugate.

For an extended target, the total scattered field is the coherent superposition of fields scattered from each scatterer, and can be written as [37], [42]

$$s_{mn}(f_k) = \iint_D \sigma(x, y)e^{-j\frac{4\pi f_k}{c}\left(\frac{R_{Tm}+R_{Rn}}{2} - R_0\right)}dxdy \tag{8}$$

where D denotes the target zone.

For a discrete array, 2-D image reconstruction can be expressed as [37], [42]

$$\hat{\sigma}(x, y) = \frac{1}{MNK}\sum_{m=1}^{M}\sum_{n=1}^{N}\sum_{k=1}^{K} s_{mn}(f_k)e^{j\frac{4\pi f_k}{c}\left(\frac{R_{Tm}+R_{Rn}}{2} - R_0\right)} \tag{9}$$

where $\hat{\sigma}(x, y)$ is the estimated scattering function at position (x, y).

III. ARRAY CALIBRATION AND AZIMUTH SIDELOBE REDUCTION

Image dynamic range is of special importance for high-resolution scattering diagnosis of complex targets. For MIMO radar near-field imaging measurement, sidelobes in the down-range dimension can be successfully reduced by applying a conventional amplitude weighting function to the frequency domain data prior to image reconstruction. However, conventional amplitude weighting approaches are not effective for azimuth sidelobe reduction. This is due to the fact that the amplitude and phase of the return data have been destroyed due to system hardware imperfection and the differences of the electrical characteristics among different channels. In this section, a novel adaptive weighting technique is proposed for the amplitude–phase error calibration of a MIMO array and azimuth sidelobe suppression.

A. Formulation

In this paper, we use the measured data of a point-like calibrator as the reference, and optimal calibration coefficients are calculated using that data and then used on the other data.

According to (7), the real return from the point calibrator can be modeled as

$$s_{mn}(f) = (1 + G_{mn}^{(e)}(f))\sigma(x, y)e^{-j\left(\frac{4\pi f}{c}\left(\frac{R_{Tm}+R_{Rn}}{2} - R_0\right) + \varphi_{mn}^{(e)}(f)\right)} \tag{10}$$

where $G_{mn}^{(e)}(f)$ and $\varphi_{mn}^{(e)}(f)$ are the gain error and the phase error of the virtual channel synthesized by the mth transmit and nth receive elements, respectively.

To calibrate the errors, a complex-valued weight $w_{mn}(f)$ is set for the output of each virtual element. The direction of arrival from the point calibrator is denoted by θ_{main} that is the mainlobe position of the point spread function (PSF) in azimuth. The calibrator position $(R, \theta_{\text{main}})$ can be obtained through measurement. Assuming that the azimuth field of view θ is equally sampled onto a discrete set $\boldsymbol{\theta} = [\theta_1, \theta_2, \ldots, \theta_Q]$, where $\theta_1 = -\theta_{\max}/2$, $\theta_Q = \theta_{\max}/2$, $\theta_{\max}$ is the maximum field of view, and $\theta_{\text{main}} \in \boldsymbol{\theta}$. The response of the MIMO array to (R, θ_q) can be written as

$$B(\theta_q) = \frac{1}{MN}\sum_{m=1}^{M}\sum_{n=1}^{N} w_{mn}(f)s_{mn}(f)e^{j\frac{4\pi f}{c}\left(\frac{R_{Tm}(\theta_q)+R_{Rn}(\theta_q)}{2}-R_0\right)} \tag{11}$$

where $q = 1, 2, \ldots, Q$,$w_{mn}(f)$ is the weight of the virtual element synthesized by the mth transmit and nth receive elements, $R_{Tm}(\theta_q) = \sqrt{R^2 + x_{Tm}^2 - 2Rx_{Tm}\sin\theta_q}$, and $R_{Rn}(\theta_q) = \sqrt{R^2 + x_{Rn}^2 - 2Rx_{Rn}\sin\theta_q}$.

For wideband signals, the electrical characteristics of each MIMO channel are not the same at different frequency point. This includes such characteristics as the phase center and gain of radiating elements, the amplitude–phase characteristics of cables, and the nonlinear behavior of individual system components. Therefore, the weight at each frequency point needs to be solved. For simplicity, we only consider the solution at the central frequency.

The PSF in azimuth at a distance R far from the center of the MIMO array can be expressed as $\mathbf{B} = [B(\theta_1), B(\theta_2), \cdots B(\theta_Q)]^T$. Then we can get, (12) shown of the bottom of the page.

Equation (12) can also be denoted as

$$\mathbf{B} = \mathbf{A}\mathbf{w}. \tag{13}$$

In our method, a vector of complex-valued weights $\mathbf{w}$ is set for the MIMO array output. The return data from each channel are weighted using the corresponding element in $\mathbf{w}$. The phase of $\mathbf{w}$ is used to calibrate the phase error of the MIMO array output, while its amplitude is used to calibrate the amplitude error of the MIMO array output as well as to suppress the azimuth sidelobes. To obtain the high-quality images, the value of $\mathbf{w}$ must include an accurate estimation of the amplitude–phase error of the MIMO array output. However, there is no analytic solution for $\mathbf{w}$ and mathematical optimization is a must.

B. Convex Optimization Solution

From [43], it is known that the absolute optimum can be obtained if a problem is convex. A convex optimization problem is the minimization of a convex function over a convex set and any local minimum is a global minimum. Therefore, we formulate the problem of solving $\mathbf{w}$ as a convex problem, then use the convex optimization algorithm to obtain the optimal solution $\mathbf{w}_{\text{opt}}$. For (12) and (13), the known values include the measured dataset $(s_{11}, s_{12}, \ldots, s_{\text{MN}})$, the main lobe position θ_{main}, and the distance R. Therefore, (13) can be divided into two parts as follows:

$$\begin{cases}\mathbf{B}_{\text{main}} = \mathbf{A}_{\text{main}}\mathbf{w}\\ \mathbf{B}_{\text{side}} = \mathbf{A}_{\text{side}}\mathbf{w}\end{cases} \tag{14}$$

where $\mathbf{B}_{\text{main}}$ is the main lobe of the PSF, $\mathbf{B}_{\text{side}}$ is the sidelobe zone in the PSF excluding from the range covered by the main lobe width, and $\mathbf{A}_{\text{main}}$ and $\mathbf{A}_{\text{side}}$ are the corresponding row vector and matrix in $\mathbf{A}$.

Based on the fact that for an ideal PSF, the mainlobe amplitude should be one (or any constant gain) while the values of sidelobes should be zero, the following equations are thus obtained:

$$\begin{cases}\mathbf{A}_{\text{main}}\mathbf{w} = 1\\ \mathbf{A}_{\text{side}}\mathbf{w} = 0\end{cases}. \tag{15}$$

Generally, no analytic solutions for $\mathbf{w}$ exist in (15). Mathematical optimization is applied to find the solution as

$$\begin{aligned}&\underset{\mathbf{w}}{\text{minmize}} \quad \|\mathbf{A}_{\text{main}}\mathbf{w} - 1\|_p\\ &\text{subject to } \|\mathbf{A}_{\text{side}}\mathbf{w}\|_1 < \varepsilon\end{aligned} \tag{16}$$

where $\|\cdot\|$ denotes the norm operator, $p = 1, 2, \infty$, and ε is the sidelobe level that is a small amount much less than one.

As can be seen, (16) is a convex optimum problem. The optimal solution $\mathbf{w}_{\text{opt}}$ is obtained using the convex optimization algorithm [43], [44].

It is expected that the amplitude of $\mathbf{w}_{\text{opt}}$ is the combination of the amplitude calibration values of the MIMO array output and a tapering function. To obtain the amplitude calibration coefficients, a process for removing the tapering function is required. To further describe this procedure, we present an example, as shown in Fig. 2. The solid line in Fig. 2(a) is the optimal amplitude weight $|\mathbf{w}_{\text{opt}}|$ obtained from the measurement data. The dashed line is the tapering function $|\mathbf{w}_{\text{opt}}^{(s)}|$ obtained from the simulation data, where simulation parameters are the same as the measurement parameters and the simulation is implemented without

$$\begin{bmatrix}B(\theta_1)\\ B(\theta_2)\\ \vdots\\ B(\theta_Q)\end{bmatrix} = \frac{1}{MN}\begin{bmatrix} s_{11}e^{j(4\pi f/c)\left((R_{T_1}(\theta_1)+R_{R_1}(\theta_1))/2-R_0\right)} & \ldots & s_{\text{MN}}e^{j(4\pi f/c)((R_{\text{TM}}(\theta_1)+R_{\text{RN}}(\theta_1))/2-R_0)}\\ s_{11}e^{j(4\pi f/c)\left((R_{T_1}(\theta_2)+R_{R_1}(\theta_2))/2-R_0\right)} & \ldots & s_{\text{MN}}e^{j(4\pi f/c)((R_{\text{TM}}(\theta_2)+R_{\text{RN}}(\theta_2))/2-R_0)}\\ \vdots & \ldots & \vdots\\ s_{11}e^{j(4\pi f/c)\left((R_{T_1}(\theta_Q)+R_{R_1}(\theta_Q))/2-R_0\right)} & \ldots & s_{MN}e^{j(4\pi f/c)\left((R_{\text{TM}}(\theta_Q)+R_{\text{RN}}(\theta_Q))/2-R_0\right)}\end{bmatrix}\begin{bmatrix}w_{11}\\ w_{12}\\ \vdots\\ w_{\text{MN}}\end{bmatrix}. \tag{12}$$

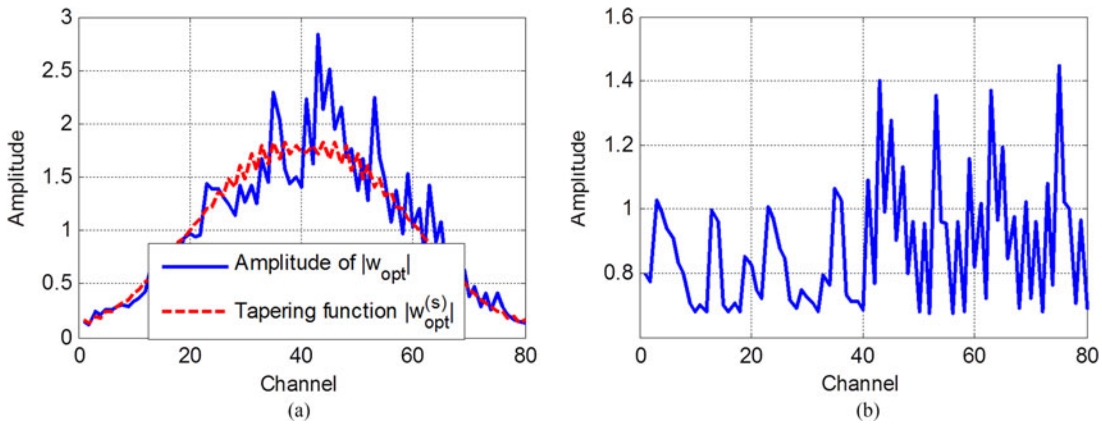

Fig. 2. Procedure for removing tapering function. (a) $|\mathbf{w}_{\rm opt}|$ and $|\mathbf{w}_{\rm opt}^{\rm (s)}|$. (b) Amplitude calibration coefficients.

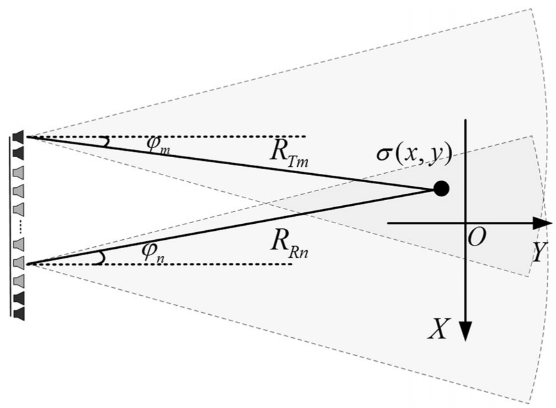

Fig. 3. Illustration of the impact of transmit and receive antenna patterns on a scatterer.

any errors. The final amplitude calibration coefficients in Fig. 2(b) are obtained by removing $|\mathbf{w}_{\rm opt}^{\rm (s)}|$ from $|\mathbf{w}_{\rm opt}|$.

IV. PRECISION IMAGING FROM NEAR-FIELD MEASUREMENTS

For near-field imaging measurement, antenna pattern is one of the main sources that impact on the accuracy. This primarily consists of two aspects, as illustrated in Fig. 3. First, for a single data acquisition channel composed of a transmit/receive antenna pair, it brings about an amplitude error of the returns from different azimuths. Second, the errors in each channel are dramatically different. Such differences result in an amplitude nonuniformity of the MIMO array output, which in turn degrades the performance of the image focusing.

Equations (8) and (9) represent an ideal model where propagation path-loss and antenna pattern are not considered. To include this, the model for returns (or the backscattered field from the target) can be modified as [45], [46]

$$s_{mn}(f_k) = \iint_D A_{Tm}(\varphi_m, f_k) A_{Rn}(\varphi_n, f_k) \times \frac{\sigma(x, y)}{R_{Tm} R_{Rn}} e^{-j\frac{4\pi f_k}{c}\left(\frac{R_{Tm}+R_{Rn}}{2} - R_0\right)} dx dy \quad (17)$$

where $A_{Tm}(\varphi_m, f_k)$ and $A_{Rn}(\varphi_n, f_k)$ are the field patterns of the mth transmit and nth receive elements at frequency point f_k, respectively, and φ_m and φ_n denote the azimuth angles of the scatterer in the beam zone of these two antenna elements, $\varphi_m = tg^{-1}((x - x_{Tm})/(y + R_0))$, $\varphi_n = tg^{-1}((x - x_{Rn})/(y + R_0))$.

Based on the inverse scattering theory [45], the image of the target scattering distribution can be obtained by coherently focusing the returns (or the scattered fields) in (17), where the focusing operator restores changes incurred by the amplitude and argument of the wave on its way to and from the scatterer. The focusing operator for a given frequency and transmit/receive element pair can be expressed as

$$\xi(x_{Tm}, x_{Rn}, f_k) = \frac{R_{Tm} R_{Rn}}{A_{Tm}(\varphi_m, f_k) A_{Rn}(\varphi_n, f_k)} e^{j\frac{4\pi f_k}{c}\left(\frac{R_{Tm}+R_{Rn}}{2} - R_0\right)}. \quad (18)$$

Considering array calibration and sidelobes suppression, the imaging model can be represented as [45]

$$\hat{\sigma}(x, y) = \frac{1}{MNK} \sum_{m=1}^{M} \sum_{n=1}^{N} \sum_{k=1}^{K} w_{mn} w_k s_{mn}(f_k) \times \frac{R_{Tm} R_{Rn}}{A_{Tm}(\varphi_m, f_k) A_{Rn}(\varphi_n, f_k)} e^{j\frac{4\pi f_k}{c}\left(\frac{R_{Tm}+R_{Rn}}{2} - R_0\right)} \quad (19)$$

where w_{mn} is the complex weight of the mnth virtual element, w_k is the real weight of the kth frequency point, and $R_{Tm} R_{Rn}$ and $A_{Tm} A_{Rn}$ are the compensation factors for amplitude decay due to the propagation path-loss and the antenna pattern tapering of element, respectively.

For simplicity, only the antenna pattern at the central frequency is used for compensation in image reconstruction, where $A_{Tm}(\varphi, f_k)$ and $A_{Rn}(\varphi, f_k)$ are denoted as $A_{Tm}(\varphi)$ and $A_{Rn}(\varphi)$, respectively.

FBP algorithm [47] is a useful tool for precise diagnostic imaging. It is adapted here for near-field MIMO radar image formation, and referred to as near-field MIMO-FBP, where the propagation path-loss, antenna pattern tapering, and phase distortion due to spherical wave front are

Fig. 4. Photo of the experimental MIMO radar.

automatically calibrated. The proposed algorithm consists of four steps.

First, the 1-D profile $P_{mn}(r)$ of return data for each channel is obtained by means of an inverse fast Fourier transform on $w_{mn}w_k s_{mn}(f_k)$.

Second, interpolation operation on $P_{mn}(r)$ is implemented to obtain the reconstruction value $P_{mn}(r')$ at position (x, y).

Third, $P_{mn}(r')$ is multiplied by the compensation factors as in the following equation:

$$\hat{\sigma}_{mn}(x, y) = \frac{R_{Tm}R_{Rn}}{A_{Tm}(\varphi_m)A_{Rn}(\varphi_n)} P_{mn}(r')e^{j4\pi f_{\min}r'/c}. \quad (20)$$

Finally, coherent summation of all $\hat{\sigma}_{mn}(x, y)$ is implemented to obtain the reconstructed value $\hat{\sigma}(x, y)$, i.e.,

$$\hat{\sigma}(x, y) = \frac{1}{MN}\sum_{m=1}^{M}\sum_{n=1}^{N}\hat{\sigma}_{mn}(x, y). \quad (21)$$

V. EXPERIMENTAL RESULTS AND DISCUSSIONS

An experimental MIMO radar, as seen in Fig. 4, is developed and a series of indoor and outdoor field tests are carried out. The X-band experimental MIMO radar operates in TDM mode. An Agilent PNA-X N5242A network analyzer is used as the transmitter as well as the receiver. TDM is implemented using RF switch matrices and will not be detailed here. The configuration of the MIMO array is the same as in Fig. 1(a), consisting of 20 receive and 4 transmit elements, where the parameter d is set as 0.05 m. The combinations among them synthesize 80 virtual elements, or 80 data acquisition channels. The gains of the transmit and the receive horn antennas are about 11 dB and 16 dB, respectively, at X-band, with 3 dB beamwidth about 38° and 26°.

In most cases, the radar frequency is set to 8–12 GHz and the frequency step is 5 MHz. If there are any changes, the new parameters will be presented again.

A. Amplitude–Phase Calibration and Sidelobe Reduction

Our first example presents the measurement results of a metallic tea urn, where the impact of the background clutter is suppressed by performing vector background subtraction. This is used to validate the performance of the proposed adaptive weighting technique.

The target is shown in Fig. 5(a) and placed at a distance of 5 m from the center of the MIMO array. An ideal 2-D PSF is calculated using the aforementioned measurement parameters, as shown in Fig. 5(b). The measured data of the tea urn are used as an input to calculate the optimal solution $\mathbf{w}_{\text{opt}}$. The value of $\mathbf{w}_{\text{opt}}$ includes an accurate estimation of the amplitude–phase error of the MIMO array output. Fig. 5(c) is the near-field MIMO image of the tea urn before calibration, which is dramatically distorted compared with Fig. 5(b). After calibration, the resulting image is presented in Fig. 5(d). As it can be seen, the image processed using the proposed method is very similar to its ideal counterpart, demonstrating that the amplitude–phase errors of the MIMO array are perfectly calibrated.

The comparison of the azimuth sidelobe suppression results using Hamming and $\mathbf{w}_{\text{opt}}$ weighting is illustrated in Fig. 6, where sidelobes in down-range dimension are reduced by applying a Hamming window to the frequency domain data. The image quality in Fig. 6(b) significantly outperforms that in Fig. 6(a), which validates that the proposed technique results in images with much lower sidelobes.

To further analyze the performances of the MIMO radar system, the amplitude and phase of the adaptive weighting $\mathbf{w}_{\text{opt}}$ are presented in Fig. 7. It can be seen that the phases of the virtual channels 1, 2, 41, and 42 are dramatically different from those of all the other channels. Detailed analysis indicates that these four virtual channels have a common receive element. We thus checked the MIMO array and found that the corresponding receive antenna waveguide was installed in a way being reverse relative to other antennas.

B. Image Calibration Accuracy

Now we address the problem of RCS image calibration. The reference is a PSF, namely, the 2-D image of a point calibrator, such as a metallic sphere or cylinder. The calibration equation can be expressed as

$$\sigma_T(x, y) = \frac{\hat{\sigma}_T(x, y)}{\hat{\sigma}_C}\sigma_C \quad (22)$$

where $\sigma_T(x, y)$ is the 2-D scattering function of the target after calibration, $\hat{\sigma}_T(x, y)$ is the original 2-D image of the target directly obtained from the measured data, $\hat{\sigma}_C$ is the maximal value of the PSF, and σ_C is the square root of the theoretical RCS of the calibrator at the central frequency.

To validate the RCS image calibration accuracy, an experiment is implemented using three classic calibrators, i.e., a metallic cylinder with a diameter of 11.43 cm and a length of 5.33 cm, and two metallic spheres with a diameter of 10 cm, as shown in Fig. 8(a). At 10 GHz, the

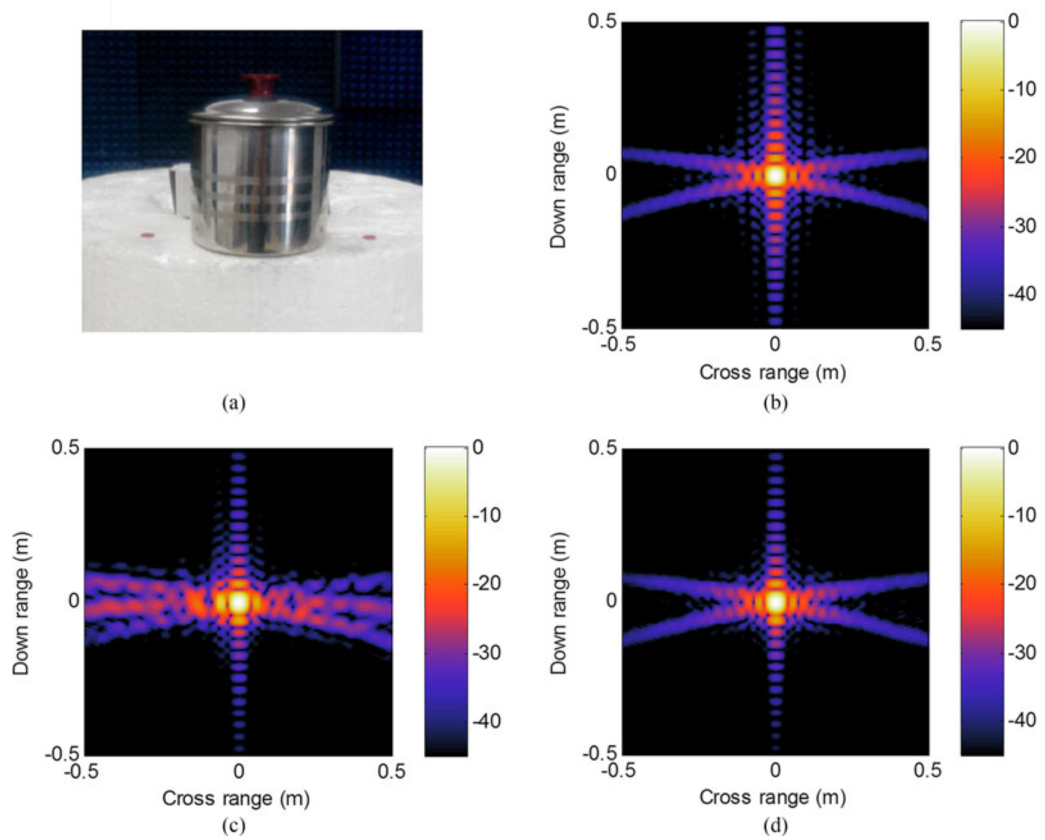

Fig. 5. Comparison of the image performances of a metallic tea urn before and after calibration. (a) Metallic tea urn. (b) Ideal PSF. (c) Before calibration. (d) After calibration.

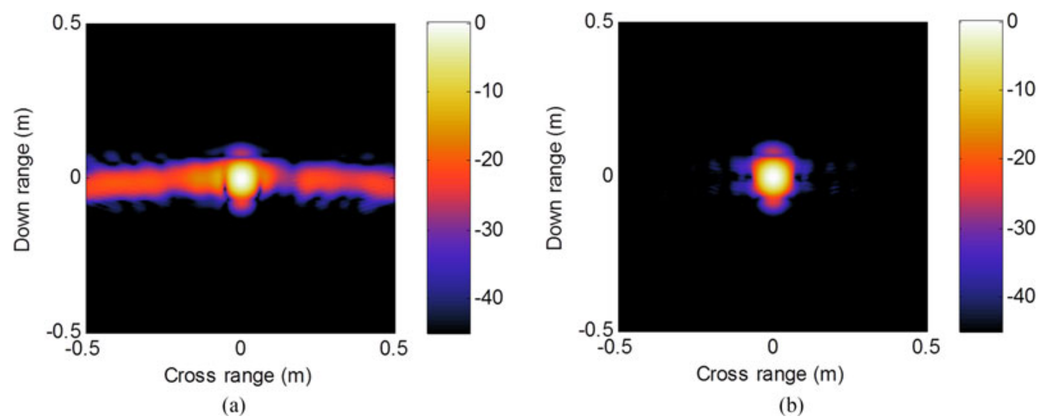

Fig. 6. Comparison of azimuth sidelobe suppression results using Hamming and $\mathbf{w}_{\text{opt}}$ weighting. (a) Hamming weighting. (b) $\mathbf{w}_{\text{opt}}$ weighting.

theoretical RCS values of the sphere and the cylinder are about –21.05 dBsm and –14.67 dBsm, respectively. The measurement scenario is illustrated in Fig. 8(b).

Fig. 9(a) is the result of RCS image calibration without compensation for the propagation path-loss and for the antenna pattern, where the maximum RCS measurement error of them is about 2.57 dB. The resulting image is formed using the near-field MIMO-FBP algorithm for a full compensation, as shown in Fig. 9(b), where the maximum error is only about 0.44 dB, demonstrating a satisfactory calibration accuracy.

C. MIMO Radar Images of Complex Targets

To further demonstrate the applicability of the currently proposed techniques, both indoor and outdoor experiments are carried out on complex targets.

For the indoor test, the target is an aircraft model with dimensions of 80 cm (D) $\times$ 40 cm (W) $\times$ 20 cm (H), placed at a distance of 5 m from the MIMO array. The calibration coefficient for the returns of the aircraft model is the $\mathbf{w}_{\text{opt}}$ calculated using the measured data of the tea urn. Sidelobes in the down-range dimension are suppressed using a Hamming window weighting to the frequency domain

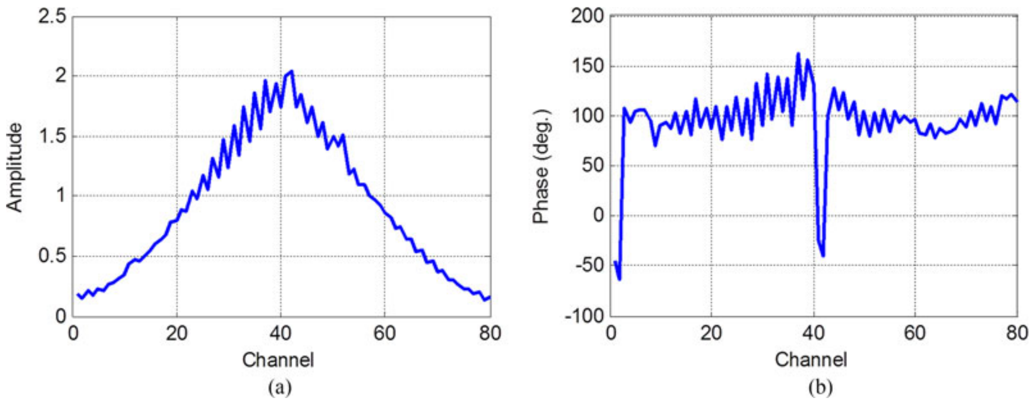

Fig. 7. Adaptive weighting vector $\mathbf{w}_{\mathrm{opt}}$. (a) Amplitude. (b) Phase.

Fig. 8. Targets and measurement scenario. (a) Metallic cylinder and spheres. (b) Measurement scenario.

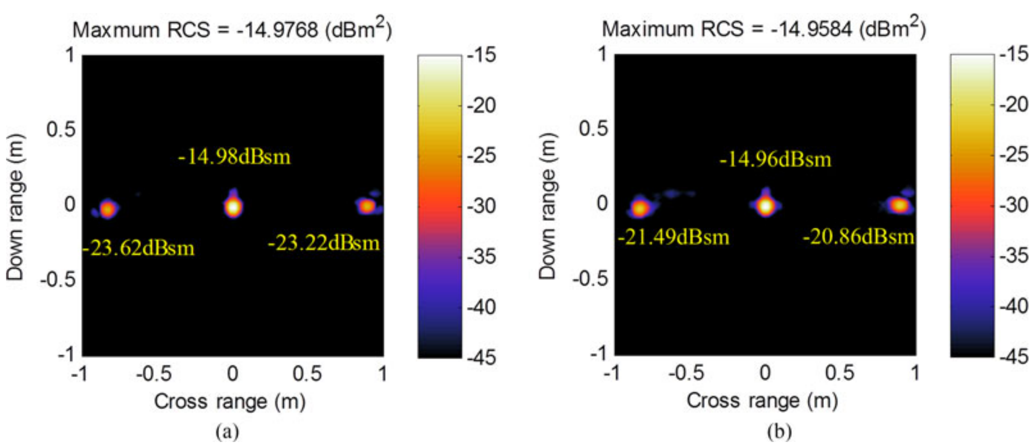

Fig. 9. Comparison of image calibration before and after compensation. (a) Before compensation. (b) After compensation.

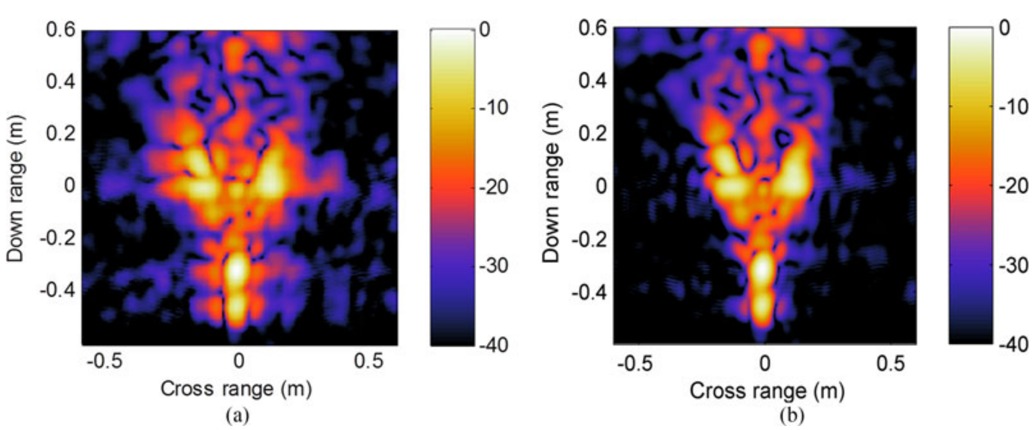

Fig. 10. Indoor experimental results of the 2-D MIMO radar images of a scaled aircraft model. (a) Hamming weighting. (b) $\mathbf{w}_{\mathrm{opt}}$ weighting.

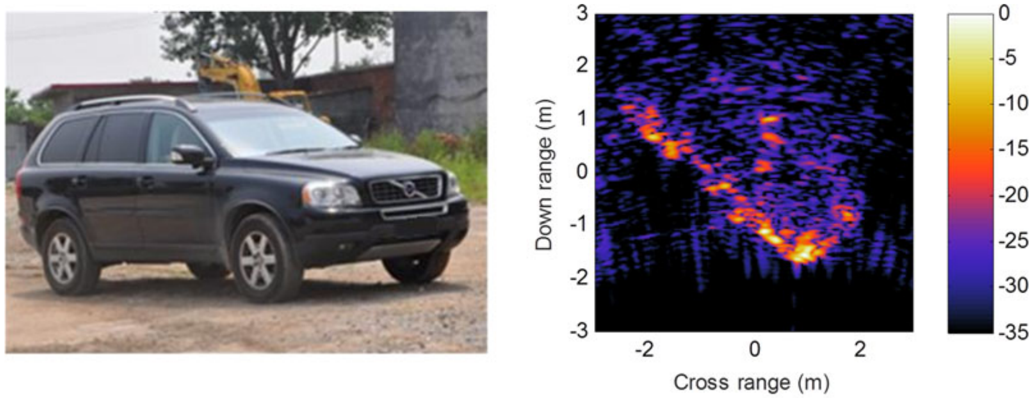

(a) (b)

Fig. 11. Outdoor experimental result of the 2-D MIMO radar image of a Volvo XC90 SUV. (a) Volvo SUV under test. (b) 2-D image.

data, while azimuth sidelobe control is accomplished via Hamming weighting and $\mathbf{w}_{\text{opt}}$ weighting to the aperture data, respectively, as shown in Fig. 10(a) and (b). It can be seen that the proposed technique results in the image with much less sidelobes, reaching a large dynamic range of 40 dB.

In the outdoor experiment, a Volvo XC90 SUV placed at a distance of 15 m from the MIMO array is selected as the target, as shown in Fig. 11(a). The measurement is implemented over an open sandy ground field. The radar frequency is set to 9–11 GHz and the frequency step is 5 MHz. Fig. 11(b) shows the resulting image. The dynamic range is now about 35 dB, lower than that for the indoor cases. This is due to the fact that the ground clutter from the sandy ground dominates the lower level of the image. It is expected that if a paved ground field is used during the measurement, the image dynamics will be improved.

VI. CONCLUSION

This paper focuses on producing high-resolution images of diagnostic quality for near-field MIMO radar imagery. Lower sidelobes and higher RCS image calibration accuracy are required. To this end, a combination of several novel image processing techniques are proposed, including the optimized adaptive weighting, the antenna pattern compensation, and the near-field MIMO-FBP imaging algorithm. Experimental results show that the proposed techniques result in greatly improved images with a dynamic range better than 40 dB, and an RCS calibration uncertainty within 1 dB, demonstrating the applicability of a MIMO radar for high-resolution diagnostic RCS imaging of complex targets.

REFERENCES

[1] I. J. LaHaie and S. A. Rice
Antenna-pattern correction for near-field-to-far-field RCS transformation of 1D linear SAR measurements
IEEE Antennas Propag. Mag., vol. 46, no. 4, pp. 177–183, Aug. 2004.

[2] G. L. Charvat, L. C. Kempel, and C. Coleman
A low-power high-sensitivity x-band rail SAR imaging system
IEEE Antennas Propag. Mag., vol. 50, no. 3, pp. 108–115, Jun. 2008.

[3] D. C. Bell and R. M. Narayanan
ISAR turntable experiments using a coherent ultrawideband random noise radar
In *Proc. IEEE Antennas Propag. Soc. Int. Symp.*, Orlando, FL, USA, Jul. 1999, pp. 1768–1771.

[4] T. Vaupel and T. F. Eibert
Comparison and application of near-field ISAR imaging techniques for far-field radar cross section determination
IEEE Trans. Antennas Propag., vol. 54, no. 1, pp. 144–151, Jan. 2006.

[5] D. J. Rabideau and P. Parker
Ubiquitous MIMO multifunction digital array radar
In *Proc. 37th Asilomar Conf. Signals, Syst., Comput.*, Nov. 2003, vol. 1, pp. 1057–1064.

[6] E. Fishler, A. Haimovich, R. Blum, D. Chizhik, L. Cimini, and R. Valenzuela
MIMO radar: An idea whose time has come
In *Proc. IEEE Radar Conf.*, Apr. 2004, pp. 71–78.

[7] K. W. Forsythe, D. W. Bliss, and G. S. Fawcett
Multiple-input multiple-output (MIMO) radar: Performance issues
In *Proc. 38th Asilomar Conf. Signals, Syst. Comput.*, Nov. 2004, vol. 1, pp. 310–315.

[8] F. C. Robey, S. Coutts, D. Weikle, J. C. McHarg, and K. Cuomo
MIMO radar theory and experimental results
In *Proc. 38th Asilomar Conf. Signals, Syst. Comput.*, Nov. 2004, vol. 1, pp. 300–304.

[9] T. Zeng, C. Miao, C. Hu, X. P. Yang, and W. M. Tian
Multi-static MIMO-SAR three dimensional deformation measurement system
In *Proc. 5th Asia-Pac. Conf. Synthetic Aperture Radar*, Singapore, Sep. 2015, pp. 297–301.

[10] J. Li and P. Stoica
MIMO radar with colocated antennas
IEEE Signal Process. Mag., vol. 24, no. 5, pp. 106–114, Sep. 2007.

[11] A. M. Haimovich, R. S. Blum, and L. J. Cimini
MIMO radar with widely separated antennas
IEEE Signal Process. Mag., vol. 25, no. 1, pp. 116–129, Jan. 2008.

[12] M. T. Frankfold, K. B. Stewart, N. Majurec, and J. T. Johnson
Numerical and experimental studies of target detection with MIMO radar
IEEE Trans. Aerosp. Electron. Syst., vol. 50, no. 2, pp. 1569–1577, Apr. 2014.

[13] C. Ma, T. S. Yeo, Z. Liu, Q. Zhang, and Q. Guo
Target imaging based on $\ell_1\ell_0$ norms homotopy sparse signal recovery and distributed MIMO antennas
IEEE Trans. Aerosp. Electron. Syst., vol. 51, no. 4, pp. 3399–3414, Oct. 2015.

[14] C. C. Gao, K. C. Teh, and A. F. Liu
Orthogonal frequency diversity waveform with range-Doppler optimization for MIMO radar
IEEE Signal Process. Lett., vol. 21, no. 10, pp. 1201–1205, Oct. 2014.

[15] M. S. Davis, G. A. Showman, and A. D. Lanterman
Coherent MIMO radar: The phased array and orthogonal waveforms
IEEE Aerosp. Electron. Syst. Mag., vol. 29, no. 8, pp. 76–91, Aug. 2014.

[16] A. D. Maio and M. Lops
Design principles of MIMO radar detectors
IEEE Trans. Aerosp. Electron. Syst., vol. 43, no. 3, pp. 886–898, Jul. 2007.

[17] A. D. Maio, M. Lops, and L. Venturino
Diversity-integration tradeoff in MIMO detection
IEEE Trans. Signal Process., vol. 56, no. 10, pp. 5501–5061, Oct. 2008.

[18] A. Aubry, M. Lops, A. M. Tulino, and L. Venturino
On MIMO detection under non-Gaussian target scattering
IEEE Trans. Inf. Theory, vol. 56, no. 11, pp. 5822–5838, Nov. 2010.

[19] Y. Yang and R. S. Blum
MIMO radar waveform design based on mutual information and minimum mean-square error estimation
IEEE Trans. Aerosp. Electron. Syst., vol. 43, no. 1, pp. 330–343, Jan. 2007.

[20] D. R. Fuhrmann and G. S. Antonio
Transmit beamforming for MIMO radar systems using signal cross-correlation
IEEE Trans. Aerosp. Electron. Syst., vol. 44, no. 1, pp. 171–186, Jan. 2008.

[21] P. Stoica, J. Li, and Y. Xie
On probing signal design for MIMO radar
IEEE Trans. Signal Process., vol. 55, no. 8, pp. 4151–4161, Aug. 2007.

[22] A. Aubry, A. D. Maio, and Y. Huang
MIMO radar beampattern design via PSL/ISL optimization
IEEE Trans. Signal Process., vol. 64, no. 15, pp. 3955–3967, Aug. 2016.

[23] J. Klare
Digital beamforming for a 3D MIMO SAR–Improvements through frequency and waveform diversity
In *Proc. IEEE Int. Geosci. Remote Sens. Symp.*, Boston, MA, USA, Jul. 2008, pp. V-17–V-20.

[24] Z. Yan, W. Liu, Q. G. Chang, and D. H. Hu
Design of a near-field radar imaging system based on MIMO array
In *Proc. IEEE Int. Conf. Electron. Meas. Instrum.*, Jul. 2015, vol. 3, pp. 1265–1269.

[25] G. L. Charvat, L. C. Kempel, E. J. Rothwell, C. M. Coleman, and E. L. Mokole
An ultrawideband(UWB) switched-antenna-array radar imaging system
In *Proc. IEEE Int. Symp. Phased Array Syst. Technol.*, Waltham, MA, USA, Oct. 2010, pp. 543–550.

[26] M. A. Ressler, L. Nguyen, F. Koenig, D. Wong, and G. Smith
The army research laboratory (ARL) synchronous impulse reconstruction (SIRE) forward-looking radar
Proc. SPIE Unmanned Syst. Technol. IX, vol. 6561, Apr. 2007, Art. no. 656105.

[27] C. Le, T. Dogaru, L. Nguyen, and M. A. Rsseler
Ultrawideband (UWB) radar imaging of building interior: Measurements and predictions
IEEE Trans. Geosci. Remote Sens., vol. 47, no. 5, pp. 1409–1420, May 2009.

[28] G. L. Charvat, L. C. Kempel, E. J. Rothwell, C. M. Coleman, and E. L. Mokole
A through-dielectric ultrawideband (UWB) switched-antenna-array radar imaging system
IEEE Trans. Antennas Propag., vol. 60, no. 11, pp. 5495–5500, Nov. 2012.

[29] J. Klare, A. Brenner, and J. Ender
A new airborne radar for 3D imaging - Image formation using the ARTINO principle
In *Proc. 6th Eur. Conf. Synthetic Aperture Radar*, Dresden, Germany, 2006, pp.1–4.

[30] M. Weiß and M. Gilles
Initial ARTINO radar experiments
In *Proc. 8th Eur. Conf. Synthetic Aperture Radar*, Jun. 2010, pp. 1–4.

[31] D. Tarchi, F. Oliveri, and P. F. Sammartino
MIMO radar and ground-based SAR imaging systems: Equivalent approaches for remote sensing
IEEE Trans. Geosci. Remote Sens., vol. 51, no. 1, pp. 425–435, Jan. 2013.

[32] P. Massaloux and P. Bérisset
Study of a near field RCS imaging system based on a MIMO array
In *Proc. Antenna Meas. Techn. Assoc.*, Atlanta, GA, USA, Nov. 2010, pp. 1–4.

[33] K. B. Stewart, N. Majurec, R. J. Burkholder, E. Ertin, and J. T. Johnson
Waveform-diverse MIMO imaging radar target measurements
In *Proc. IEEE Radar Conf.*, May 2014, pp. 918–922.

[34] M. T. Frankford, N. Majurec, and J. T. Johnson
Software-defined radar for MIMO and adaptive waveform applications
In *Proc. IEEE Radar Conf.*, 2015, pp. 1590–1594.

[35] M. Cattenoz and P. Brouard
An experimental demonstration of a posteriori digital calibration of MIMO radar system
In *Proc. Int. Radar Conf.*, 2014, pp. 1–5.

[36] J. H. G. Ender and J. Klare
System architectures and algorithms for radar imaging by MIMO-SAR
In *Proc. IEEE Radar Conf.*, May 2009, pp. 1–6.

[37] Y. Z. Liu and X. J. Xu
Azimuth sidelobe suppression technique for near field MIMO radar imaging
Proc. SPIE Image Signal Process. Remote Sens. XXI, vol. 9643, Sep. 2015, Art. no. 96431E.

[38] X. D. Zhuge and A. G. Yarovoy
A sparse aperture MIMO-SAR-based UWB imaging system for concealed weapon detection
IEEE Trans. Geosci. Remote Sens., vol. 49, no. 1, pp. 509–518, Jan. 2011.

[39] X. D. Zhuge and A. G. Yarovoy
Three-dimensional near-field MIMO array imaging using range migration techniques
IEEE Trans. Image Process., vol. 21, no. 6, pp. 3026–3033, Jun. 2012.

[40] Z. Li, T. Jin, B. Chen, and Z. M. Zhou
A coarray based MIMO array design method for UWB imaging
In *Proc. IET Int. Conf. Radar Syst.*, Oct. 2012, pp. 1–5.

[41] N. Levanon
Stepped-frequency pulse-train radar signal
Proc. IEE, Radar, Sonar Navig., vol. 149, no. 6, pp. 297–309, Dec. 2002.

[42] T. Spreng, U. Prechtel, B. Schonlinner, V. Ziegler, A. Meusling, and U. Siart
UWB near-field MIMO radar: Calibration, measurements and image reconstruction
In *Proc. 10th Eur. Radar Conf.*, Nuremberg, Germany, Oct. 2013, pp. 33–36.

[43] H. Lebret and S. Boyd
Antenna array pattern synthesis via convex optimization
IEEE Trans. Signal Process., vol. 45, no. 3, pp. 526–532, Mar. 1997.

[44] M. Grant and S. Boyed
CVX: MATLAB software for disciplined convex programming 2014. [Online]. Available: http//:cvxr.com/cvx

[45] A. Broquetas, J. Palau, L. Jofre, and A. Cardama
Spherical wave near-field imaging and radar cross-section measurement
IEEE Trans. Antennas Propag., vol. 46, no. 5, pp. 730–735, May 1998.

[46] Y. Z. Liu and X. J. Xu
Antenna pattern compensation technique for near field MIMO radar imaging
In *Proc. Int. Conf. Electromagn. Adv. Appl.*, Sep. 2016, pp. 385–388.

[47] J. X. Lopez and Z. J. Qiao
Filtered back projection inversion of turntable ISAR data
Proc. SPIE Algorithms Synthetic Aperture Radar Imagery XVIII, vol. 8051, 2011, Art. no. 805109.

Yongze Liu was born in Hebei, China, in 1980. He received the B.S. degree in electronic and information engineering from Hebei Normal University, Shijiazhuang City, China, in 2003, and the M.S. degree in electronic and information engineering from Changchun University of Science and Technology, Changchun City, China, in 2006. He is currently working toward the Ph.D. degree in signal and information processing in the School of Electronic and Information Engineering, Beihang University, Beijing, China.

From 2006 to 2009, he was a Lecturer in the College of Physics and Information Engineering, Hebei Normal University, Hebei, China. His research interests include MIMO radar imagery and RCS measurement.

Xiaojian Xu was born in Jiangxi, China, in 1963. He received the B.S. degree from Hefei University of Technology, Hefei, China, in 1983, the M.S. degree from Beijing Institute of Environmental Features (BIEF), Beijing, China, in 1986, and the Ph.D. degree from the University of Nebraska–Lincoln, Lincoln, NE, USA, in 2002, all in electrical engineering.

From 1986 to 1999, he was with the BIEF, where he was mainly involved in research of electromagnetic scattering modeling and microwave imaging. From June 1999 to December 2002, he was with the Environmental Remote Sensing Laboratory, University of Nebraska–Lincoln, where his main research work was on ultrawideband random noise radar with emphasis on foliage and ground-penetration applications. Since January 2003, he has been with the School of Electronic and Information Engineering, Beihang University, Beijing, China, as a Signal and Information Processing Professor. His research interests mainly include remote sensing signatures, radar imagery, target recognition, and system modeling.

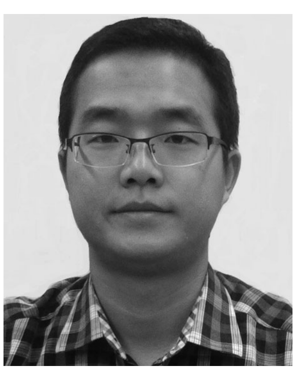

Guangyao Xu was born in Shanxi, China, in 1986. He received the B.S. degree in electrical engineering from Hefei Electronic Engineering of Institute, Hefei, China, in 2008. He is currently working toward the M.S. degree in signal and information processing in the School of Electronic and Information Engineering, Beihang University, Beijing, China.

His research interests include SAR imagery and scattering diagnosis.